THE UNIVERSITY of EDINBURGH

Edinburgh Research Explorer

Central nervous system regeneration is driven by microglia necroptosis and repopulation

Citation for published version:
Lloyd, AF, Davies, CL, Holloway, RK, Labrak, Y, Ireland, G, Carradori, D, Dillenburg, A, Borger, E, Soong, D, Richardson, JC, Kuhlmann, T, Williams, A, Pollard, JW, des Rieux, A, Priller, J & Miron, VE 2019, 'Central nervous system regeneration is driven by microglia necroptosis and repopulation', *Nature Neuroscience*, vol. 22, no. 7, pp. 1046–1052. https://doi.org/10.1038/s41593-019-0418-z

Digital Object Identifier (DOI):
10.1038/s41593-019-0418-z

Link:
Link to publication record in Edinburgh Research Explorer

Document Version:
Peer reviewed version

Published In:
Nature Neuroscience

Publisher Rights Statement:
This is the authors' peer-reviewed manuscript as accepted for publication.

General rights
Copyright for the publications made accessible via the Edinburgh Research Explorer is retained by the author(s) and / or other copyright owners and it is a condition of accessing these publications that users recognise and abide by the legal requirements associated with these rights.

Take down policy
The University of Edinburgh has made every reasonable effort to ensure that Edinburgh Research Explorer content complies with UK legislation. If you believe that the public display of this file breaches copyright please contact openaccess@ed.ac.uk providing details, and we will remove access to the work immediately and investigate your claim.

OPEN ACCESS

Download date: 06. May. 2023

Nature Neuroscience: Brief Communication

Title: Central nervous system regeneration is driven by microglia necroptosis and repopulation

Authors: Amy F. Lloyd[1], Claire L. Davies[1], Rebecca K. Holloway[1], Yasmine Labrak[2], Graeme Ireland[1], Dario Carradori[2], Alessandra Dillenburg[1], Eva Borger[3], Daniel Soong[1], Jill C. Richardson[4], Tanja Kuhlmann[5], Anna Williams[3], Jeffrey W. Pollard[1], Anne des Rieux[2], Josef Priller[6,7], Veronique E. Miron[1]*

Affiliations:

[1] Medical Research Council Centre for Reproductive Health, The Queen's Medical Research Institute, The University of Edinburgh, Edinburgh, Scotland, United Kingdom, EH16 4TJ.

[2]Louvain Drug Research Institute, Advanced Drug Delivery and Biomaterials, Université Catholique de Louvain, Avenue Mounier, 73, B1 73.12, 1200 Brussels, Belgium.

[3]Medical Research Council Centre for Regenerative Medicine, The University of Edinburgh, Edinburgh, Scotland, United Kingdom, EH16 4UU.

[4]Neurosciences Therapeutic Area Unit, GlaxoSmithKline R&D Ltd, Stevenage, England, United Kingdom, SG1 2NY.

[5]Institute of Neuropathology, University Hospital Muenster, Muenster, Germany, 48149.

[6]Department of Neuropsychiatry and Laboratory of Molecular Psychiatry, Charité Universitätsmedizin Berlin, Charitéplatz 1, 10117 Berlin, Germany.

[7]United Kingdom Dementia Research Institute, The University of Edinburgh, Edinburgh, Scotland, United Kingdom, EH16 4TJ.

***Correspondence to:**
Veronique E. Miron
Medical Research Council Centre for Reproductive Health
The Queen's Medical Research Institute
47 Little France Crescent
Edinburgh, Scotland, United Kingdom
EH16 4TJ
Email: vmiron@ed.ac.uk

Abstract:

Failed regeneration of central nervous system myelin contributes to clinical decline in neuroinflammatory and neurodegenerative diseases, for which there is an unmet therapeutic need. Here, we reveal that efficient remyelination requires death of pro-inflammatory microglia followed by repopulation to a pro-regenerative state. We propose that impaired microglia death and/or repopulation may underpin dysregulated microglia activation in neurological diseases, and reveal novel therapeutic targets to promote white matter regeneration.

Main text:

Central nervous system (CNS) remyelination reinstates axon health and function[1-3], yet fails in prevalent neurodegenerative disorders contributing to axon dysfunction/loss[4-6] for which there is an unmet therapeutic need. These disorders (e.g. multiple sclerosis, ALS, spinal cord injury) are associated with chronic activation of the resident immune cells, microglia[7-10]. Effective resolution of pro-inflammatory microglia activation (iNOS+ TNFα+ CCL2+) via a transition to a pro-regenerative microglia state (Arg-1+ CD206+ IGF-1+) initiates remyelination[8]. Remyelination is impaired when this transition is either prevented (by targeted depletion of pro-regenerative microglia), or when it fails, as identified by prolonged pro-inflammatory microglia presence in aged mice and chronic human brain lesions[8]. However, the mechanisms underpinning this transition in microglia activation remain unknown.

To reveal these mechanisms, we performed RNA sequencing of microglia isolated from focal demyelinated lesions of young adult mouse corpus callosum induced with the myelin toxin lysophosphatidyl choline (LPC), where regeneration occurs without concomitant damage and the timing of microglia activation has been previously defined (Fig. 1A)[8]. At the peak of pro-inflammatory (3 dpl) and pro-regenerative microglia activation (10 dpl), microglia were FACS-isolated based on expression of CD11b, lack of expression of neutrophil and T lymphocyte markers (Ly6G, CD3), and low expression of CD45 (gating strategy in Supplementary Fig.1A); use of differential CD45 expression (on the logarithmic scale) to distinguish between microglia (lo) and infiltrating monocyte-derived macrophages (hi) in white matter injury has been previously validated using transgenic reporters and bone marrow chimeras[11-15]. Cells expressed microglia signature genes at both time points post-demyelination (Supplementary Fig.1B); we assessed regulation of two of these genes (*P2ry12*, *Csf1r*) after demyelination versus non-lesion microglia by qPCR, and observed no significant change at 3 dpl yet subsequent upregulation at 10 dpl (Supplemental Fig.1C). Cells did not express markers for border-associated macrophages or monocyte-derived cells[16,17](Supplementary Fig.1D). Of the 5000 most highly expressed genes for each time point (including non-differentially expressed genes), 57.2% were shared and 21.4% were specific to each time point (Fig. 1B). Microglia

also expressed some genes associated with neonatal microglia during developmental myelination[18,19] (Supplementary Fig. 1E, F) or adult microglia during neurodegeneration[20,21] (Supplementary Fig. 1G-I), some of which were significantly enriched in microglia at 10 dpl. 1020 genes were significantly differentially expressed between 3 and 10 dpl ($p<0.05$) (Fig. 1C; Log_2 fold change in Supplementary Sheet 1), indicating differing functions. These included genes involved in survival/ proliferation (*Birc5*, *Smad2*, *Ccnb1*), anti-oxidant responses (*Keap1*), inflammation (*Tnfrsf1b*, *Jak2*, *Nfkbid*, *Cryba1*, *Gpmnb*, *Socs1*, *Cd40*), remyelination (*Axl*, *Osm*, *Adam8*), and associated with microglia in neurodegeneration (*Msr1*, *Hdac5*, *Syp*) (Supplementary Fig. 1J). Gene Ontology (GO) term enrichment analysis identified differential regulation of the immune response, with 3 dpl microglia showing '*positive regulation of chronic inflammatory responses*', whereas 10 dpl microglia showed '*positive regulation of Th2 cell cytokine production*', '*positive regulation of IL-10 secretion*', and '*positive regulation of IL-13 secretion*' (Supplementary Fig. 2), suggesting pro- and anti-inflammatory functions, respectively. Accordingly, transcriptional regulators upregulated at 10 dpl [identified using Ingenuity Pathway Analysis (IPA)] included those with anti-inflammatory function (*Bcl6*, *Grhl1*, *Tle1*, *Nfkbid*) (Supplementary Table 1; Supplementary Fig. 1K). Significantly upregulated genes at 10 dpl included those previously shown to directly regulate remyelination/ nervous system regeneration (*Matn2*, *Osm*, *Fgf1*, *Cd300lf*), those associated with myelination (*Bmp1*, *Cd69*, *Fabp5*), and those which control pathways that support oligodendrocyte lineage cell responses [iron export (*Cp*), Wnt pathway inhibition (*Nit1*)] (Fig.1D, Supplementary Fig. 1L). This suggests a complex contribution of pro-regenerative microglia to remyelination via establishment of a supportive microenvironment. Both 3 dpl and 10 dpl microglia showed significant engagement of phagocytic pathways, as identified by KEGG analysis ('*fat digestion'* at 3 dpl; '*endocytosis'* at 10 dpl; Fig. 1E) and GO terms (e.g. *'degradation of lipoproteins'* at 3dpl; *'structural constituent of myelin sheath'* at 10 dpl; Supplementary Fig.2), suggesting engulfment and/or breakdown of myelin debris throughout remyelination, as previously shown[22-24]. Accordingly, receptors associated with myelin debris phagocytosis during remyelination were expressed at both time points (Fig. 1F).

We found enrichment of cell death-associated pathways in microglia at 3 dpl. First, KEGG pathway analysis identified *'axon guidance'* and *'colorectal cancer'* pathways to be engaged which were associated with genes regulating cell death (*Birc5*, *Smad2*, *Ephrb1/2*) (Fig. 1E). Second, IPA analysis identified '*Cell death & Survival*' as a major molecular and cellular function (Fig. 1G), due to regulation of genes associated with death pathways such as TNF receptor signalling[25], TRAIL[26], and p53 (Supplementary Table 2). Third, the majority of transcriptional regulators upregulated at 3 dpl are known to control cell death (Supplementary Table 1; Supplementary Fig. 1M). To determine whether microglia undergo death after demyelination, we analysed IBA-1+ cells in lesions. We observed a change in the distribution of IBA-1+ cells over time, which was homogenous at 3 dpl, sparse at 7 dpl, and clustered at 10 dpl (Fig. 1I). The density of IBA-1+ cells was decreased at 7 days post-LPC (dpl) (Fig.1H, I), a time intermediate to the peaks in pro-inflammatory microglia (3 dpl) and pro-regenerative microglia (10 dpl), such that this was no longer significantly different from sham control. This represented cell death, as flow cytometric analysis of microglia ($Cd11b^{+}$ $Cd45^{lo}$) death (Annexin-V+ 7-AAD+) revealed an increase at 7 dpl (Fig. 1J, K; gating strategy Supplementary Fig. 3A; Supplementary Fig. 3C). Microglia isolated from sham-lesioned mice at 7 days post-surgery were negative for Annexin-V and 7-AAD (Supplementary Fig. 3B), excluding the possibility that death occurred consequent to injection or cell isolation. Thus, after demyelination and prior to onset of efficient remyelination, microglia die during the transition from pro-inflammatory to pro-regenerative activation.

To investigate mechanisms regulating microglia death after demyelination, we first used *ex vivo* mouse organotypic cerebellar slice cultures which mimic the tissue microenvironment and remyelination seen *in vivo*[27], yet are amenable to precise time courses and live imaging of deep brain white matter (Supplementary Fig. 4A). Consistent with observations *in vivo*, microglia (CD68+, PU.1+, IBA-1+) in LPC-demyelinated slices were decreased by 1 dpl, intermediate to the peaks in pro-inflammatory microglia (iNOS+ CD68+; 0.5 dpl) and pro-regenerative microglia (Arg-1+ CD68+; 7 dpl) (Supplementary Fig. 4B-F). Vehicle (PBS)-treated explants showed no demyelination (Supplementary Fig. 4G) nor iNOS+ CD68+ cells (Supplementary Fig.4H) at any time, with MBP

immunoreactivity comparable to fully myelinated untreated slices (Supplementary Fig. 4I). Live incorporation of a marker of compromised membrane integrity (propidium iodide; PI) confirmed microglia death prior to cell loss (18-24 hours post-LPC (hpl); Supplementary Fig. 4J-M) and PI was present in the vast majority of PU.1+ microglia nuclei by 24 hpl (Supplementary Fig. 4M). We ruled out microglia death via toxic effects of LPC, as no cell loss was observed when primary microglia cultures were treated with LPC overnight (Supplementary Fig. 5A). Live imaging of explants derived from mice in which microglia are eGFP+ (*Csf1r*-eGFP; MacGreen) showed microglia rounding up and rupturing post-LPC, which was not observed in non-demyelinated explants (Supplementary Videos S1, S2). However, microglia were negative for the apoptotic markers cleaved caspase-3 and TUNEL (Supplementary Fig. 5B), yet constitutively positive for the pyroptosis marker cleaved caspase-1 (Supplementary Fig. 5C) suggesting the involvement of the latter in non-death-associated pathways[28]. We then investigated necroptosis, a programmed necrosis whereby a necroptosome complex composed of RIPK1, RIPK3, and MLKL compromises membrane integrity[29,30]. Necroptosis markers were expressed in IBA-1+ or CD68+ cells after demyelination at time points prior to their death: at 3 dpl *in vivo* (Fig. 2A-C; Supplementary Fig.5D; IBA-1 and MLKL co-localization: 34.2 % at 3 dpl vs 7.0 % at 7 dpl) and 12 hpl in slices (Fig. 2D, E). Although some CD68+ cells were present in sham-injected mice *in vivo*, these were RIPK3-negative (Fig. 2A). Additionally, several genes that regulate necroptosis were enriched in the '*Cell death & Survival*' pathways identified by IPA analysis (*Tnfsf10*, *Gadd45a*, *Jak2*, *Socs1*, *Bcl3*, *Birc5*, *Cd40*, *Ppm1d*, *Rcan1*, *Tnfrsf1b*, *Msra*, *Slamf7*, *Comp*, *Hspa1b*) (Supplementary Table 2). Using lineage tracing of infiltrating monocyte-derived macrophages via *Ccr2*-driven RFP expression, we confirmed that the majority of RIPK3+ cells in lesions *in vivo* were RFP- rather than blood monocyte-derived (RFP+) (Supplementary Fig. 6A-C). Additionally, CD68 staining in lesions strongly co-localized with the microglial marker Tmem119 (Supplementary Fig.6D, E). We confirmed that microglia necroptosis is a common feature of remyelination by analysing 2 additional *in vivo* models of demyelination. In the cuprizone toxin-diet model[31], RIPK3+ and MLKL+ microglia were significantly increased at the onset of remyelination, and decreased once remyelination was complete at 4 weeks on normal diet (Supplementary Fig. 7A-D). Mining of published study on microglia transcriptomes from a model of chronic myelin injury to

the spinal cord [MOG-induced experimental autoimmune encephalomyelitis (EAE)][32] indicated expression of both *Ripk3* and *Mlkl* at late stages of disease, when remyelination takes place in this model[33] (Supplementary Fig. 7E). Therefore, microglia necroptosis appears to be associated with the onset of remyelination, regardless of CNS region or mode of injury.

To determine the role of microglia necroptosis in remyelination, we used necrostatin-1, a small molecule which prevents necroptosome activity[34]. At 1 dpl, necrostatin-1 treatment of demyelinated slices prevented the loss of CD68+ microglia (Fig. 2F) and maintained iNOS+ CD68+ microglia numbers (Fig. 2G-H). The latter were still prominent at 7 dpl when the transition to the pro-regenerative phenotype would normally have taken place (Fig. 2G, H); we did however observe a subsequent decrease in iNOS+ CD68+ cell numbers by 14 dpl (Fig. 2G) which may indicate either a delayed change in activation or apoptosis as a consequence of prolonged necroptosis inhibition[35]. Importantly, necrostatin-1 treatment significantly hindered remyelination at 7 and 14 dpl compared to the robust remyelination observed in the vehicle control (Fig. 2I, J). This effect did not result from directly inhibiting oligodendrocyte or neuronal necroptosis, documented during prolonged experimental demyelination/ in multiple sclerosis cortical lesions[36] or in Alzheimer's disease[37], respectively, as only ~3% of oligodendrocyte lineage cells (Olig2+) or neurons (NeuN+) were RIPK3+ post-LPC in slices (Supplementary Fig. 8A-D). We confirmed that necrostatin-1 treatment in undemyelinated slices had no consequence on MBP immunoreactivity or iNOS expression in CD68+ microglia (Supplementary Fig.8E, F). To determine whether microglia necroptosis is also required for efficient remyelination *in vivo*, we aimed to specifically target necrostatin to macrophages by encapsulation in lipidic nanocapsules (LNCs) which were predicted to be preferentially taken up by phagocytes, as has been shown with other lipid-rich nanoparticle formulations[8,22,38,39] (Fig.2K). Specificity of uptake in lesions was verified by injection of DiD-labelled LNCs, with >90% of DiD clusters co-localized with IBA-1+ cells (Fig.2L, N), significantly more than the percentage of clusters co-localized with other cell types with phagocytic capacity [3.9% of clusters in astrocytes (GFAP+; Fig. 2L, N) and 1.3% of clusters in oligodendrocyte lineage cells (CC1+, Olig1+; Fig.2N, Supplementary Fig. 8G, H)]. 3D reconstruction confirmed the internalization of DiD-LNCs within IBA-1+ cells (Fig. 2M; Supplementary Fig.8H). At 3 dpl, necrostatin-loaded LNCs inhibited

144 microglia necroptosis as indicated by decreased MLKL staining in IBA-1+ cells compared to vehicle
145 (DMSO)-LNCs (Fig. 2O), reducing co-localization of MLKL and IBA-1 from 45.11% to 20.93%.
146 Necrostatin-LNCs did not affect percentage of RIPK3+ CD68+ cells (Supplementary Fig. 8I), as
147 expected given that necrostatin does not prevent RIPK3 expression but rather acts downstream to
148 inhibit MLKL recruitment and activation[40,41]. Necrostatin-LNCs caused a relative increase in the
149 number of Tmem119+ cells compared to vehicle LNCs (Fig. 2P), associated with an increased
150 percentage of CD68+ cells expressing iNOS and decreased percentage of those expressing Arg-1 (Fig.
151 2P). The increased microglia number was not consequent to enhanced proliferation, as Ki67+ PU.1+
152 cell number was significantly downregulated at 3 dpl in Necrostatin-LNC-treated lesions relative to
153 vehicle-LNC control, then negligible in both conditions by 10 dpl (Supplementary Fig. 8J).
154 Remyelination was impaired at 10 dpl following necrostatin-LNC treatment as indicated by reduced
155 expression of the early remyelination marker myelin associated glycoprotein (MAG) (Fig.2Q, R).
156 This impairment was not due to accumulation of myelin debris (identified using MBP which is not yet
157 expressed at this early stage of remyelination) which was equally cleared in both LNC-treatment
158 conditions (Supplementary Fig. 8K), consistent with our RNA sequencing data suggesting phagocytic
159 capacity of pro-inflammatory microglia (Fig.1E, F; Supplementary Fig.2). Altogether, this data
160 demonstrates the requirement for microglia necroptosis for efficient remyelination to take place.
161 Having shown that lesion microglia die early-on following demyelination, we next
162 determined how these repopulate to the pro-regenerative phenotype. We first assessed Nestin
163 expression, shown to identify repopulating microglia following their experimental depletion in
164 healthy brain[42-44]. *In vivo* focal lesions of the corpus callosum showed an increase in co-localization of
165 IBA-1 with Nestin from 3 dpl to 7 dpl, which was reduced by 10 dpl when the transition in microglia
166 activation has taken place (Fig. 3A-C). Little to no Nestin was co-localized with IBA-1 in sham
167 control, indicating its expression by microglia largely during remyelination (Fig.3A). Microglia
168 repopulation following experimental depletion has been proposed to occur via two mechanisms: i) *de*
169 *novo* differentiation of CNS-resident Nestin+ cells[43], or ii) proliferation of residual microglia which
170 did not die[42,44]. However, these studies only examined microglia repopulation in otherwise healthy
171 grey matter, where the microenvironment is likely to differ from focally injured white matter. Thus, to

determine to what extent these mechanisms account for microglia repopulation following demyelination, we performed lineage tracing. We induced focal lesions *in vivo* in mice in which Nestin promoter-driven tdTomato (tdT) expression is inducible (*Nes*-CreERT2;RCL-tdT), allowing labelling of Nestin+ cells prior to demyelination. Of all tdT+ cells, the proportion which were $Cd11b^{+}$ $Cd45^{lo}$ (gating Supplementary Fig. 9A) increased from 3 dpl to 7 and 10 dpl (Fig. 3D, E; Supplementary Fig. 9B). Although the proportion of all $Cd11b^{+}$ $Cd45^{lo}$ cells which were tdT+ was increased at 7 dpl in comparison to 3 dpl and sham control, these only represented <5% of total microglia (Fig. 3F, G) suggesting that repopulation *in vivo* is mediated primarily by residual microglia.

In the *ex vivo* model, we observed repopulation of both CD68+ cells (Supplementary Fig.4C) and PU.1+ cells (from 17 ± 3 cells/field at 24 hpl to 38 ± 1 cells/field at 3 dpl). Following 4-hydroxytamoxifen-induced tdT expression in Nestin+ cells in slices derived from *Nes*-CreERT2;RCL-tdT mice (recombination prior to LPC treatment; Supplementary Fig. 9C, D), we detected tdT+ IBA-1+ cells only during repopulation (1-2 dpl), albeit at a higher proportion than observed *in vivo* (35% of all IBA-1+ cells at 2 dpl) (Supplementary Fig.9E, F). However, their presence was transient as they were not detected by 7 dpl (Supplementary Fig. 9E). Interestingly, tdT+ cells expressed neural stem cell markers Musashi-1 and Sox2, but were negative for GFAP (Supplementary Fig.9G). As a large proportion of IBA-1+ microglia were tdT negative, we assessed the contribution of residual microglia to repopulation using slices derived from *Cx3cr1*-CreER; RCL-tdT mice, in which tdT expression was induced in CX3CR1+ cells by 4-OHT (Supplementary Fig. 9H). tdT expression was detected in IBA-1+ microglia (Supplementary Fig. 9I) but not the oligodendrocyte lineage which has been suggested to express CX3CR1[45] (Supplementary Fig. 9J). We confirmed that the majority of repopulated IBA-1+ cells were tdT+ and therefore derived from residual microglia (Supplementary Fig.9K-M); Approximately 30% of the tdT+ cells were Nestin+ at 2dpl (Supplementary Fig.9N, O). As the entire explant is a lesion due to blanket LPC exposure, we can infer that repopulation following demyelination can occur from microglia within injured areas and does not require recruitment of microglia from non-lesion areas. Therefore, our lineage tracing supports that microglia repopulation during remyelination occurs primarily from residual microglia.

To investigate myeloid cell necroptosis and repopulation in human white matter disease, we examined multiple sclerosis (MS) lesion subtypes: i) active lesions, which have high densities of macrophages, positively correlated with remyelination[46,47] and oligodendrocyte precursor abundance[48], ii) chronic inactive lesions, which have low potential for remyelination, and iii) fully remyelinated lesions (Supplementary Table 3). Although densities of CD68+ cells undergoing necroptosis (RIPK3+ and MLKL+; Fig. 3H, I, K) or PU.1+ cells undergoing repopulation (Nestin+; Fig. 3J, L) were present in all MS lesion types, these were only significantly increased in active lesions compared to control tissue. This may suggest abundance of permissive cues for pro-remyelination microglial responses in an inflammatory environment.

We next investigated molecular pathways controlling microglia behaviour during remyelination. IPA analysis indicated Type-1 interferon (IFN) signalling as being significantly regulated in microglia during remyelination, with '*Interferon signalling*' and '*Role of JAK1, JAK2, and TYK2 signalling in Interferon signalling*' identified as top canonical pathways, and top predicted upstream regulators included IFNα/β, IFNAR, STAT1, IRF7, and IRF3 (P=0.00013, 0.00089, 0.000045, 0.0071, 0.000086, respectively). We observed expression of the genes encoding the two chains of the IFN α/β receptor (*Ifnar1*, *Ifnar2*) and IFN-associated genes previously linked with microglia during remyelination[49] (Supplementary Fig. 10A, B); The IFN receptor subunit IFNAR2 was detected at the protein level in CD68+ cells in remyelinating lesions *in vivo* (Fig. 3M). IFN signalling, assessed by nuclear phospho-STAT1, was only active at 7 dpl *in vivo* and this was selective to PU.1+ nuclei (Fig. 3N). Only a subpopulation of PU.1+ nuclei were phospho-STAT1+ at 7 dpl (58 ± 7%; Fig.3O), consistent with a recent single-cell sequencing study of microglia in this model at this time point which showed that the largest microglia sub-cluster (~60% of total) has an interferon signature [49]. Given that at 7 dpl in the *in vivo* model microglia death and repopulation are concurrent, we assessed the role of Type-1 IFN signalling in either process using the brain explant demyelination model where these two responses are temporally separated (Supplementary Fig. 4C) and can thus be investigated in isolation. We blocked IFN receptor function using a neutralizing antibody against IFNAR2 and investigated effects on microglia number at the peak of microglia death (1 dpl) and repopulation (7 dpl) in explants. Anti-IFNAR2 treatment did not significantly affect

PU.1+ microglia numbers at 1 dpl compared to IgG isotype control (Fig. 3P), therefore did not prevent microglia death. However, a significant increase in PU.1+ cells from 1 dpl to 7 dpl was observed in control conditions but not following IFNAR2 blockade (Fig. 3P), suggesting impaired microglia repopulation in the latter. PU.1+ cells were significantly reduced in anti-IFNAR2 IgG conditions relative to control at 7 dpl (Fig. 3P, Q), and IBA-1+ cells were reduced to 37% of control (± 21) at this time. This was associated with a significant decrease in phospho-STAT1+ PU.1+ microglia at the peak of repopulation (7 dpl; Supplementary Fig. 10C), indicating effective inhibition of IFN signalling in microglia with IFNAR2 neutralization. Consequently, blocking IFNAR2 impaired early remyelination at 7 dpl relative to control (Fig. 3R, S). Altogether, this data supports a regenerative role for Type-1 IFN signalling in regulating the repopulation of white matter microglia during efficient remyelination.

In summary, our data reveal that remyelination is driven by coordination of pro-inflammatory microglia necroptosis and repopulation to a regenerative state. Whereas necroptosis of other cell types such as oligodendrocytes[36] and neurons[37] is associated with demyelination and neurodegeneration, respectively, here we show a novel regenerative role for necroptosis in rapidly shutting down pro-inflammatory microglial activation to support remyelination. Although previous studies identified the capacity of microglia to repopulate following experimental depletion in healthy[42-44], aged[50], irradiated[51], or neurodegenerating brain[52], we now show that this feature can also serve to reinstate the microglia population after naturally occurring death following white matter injury, while regulating microglia activation. We reveal that microglia repopulation during white matter remyelination is positively regulated by Type-1 IFN signalling. This contrasts with its deleterious role in repopulated microglia selectively in grey matter following experimental depletion[53]- highlighting CNS region-specific consequences of IFN signalling in microglia[53,54]- and complements findings of an IFN signature in microglia during recovery from facial nerve axotomy[55]. We propose that targeting pro-inflammatory microglia death in neurological diseases may represent a novel strategy to dampen chronic CNS white matter inflammation, and support a regenerative response to reinstate myelin integrity.

References:

1 Irvine, K. & Blakemore, W. Remyelination protects axons from demyelination-associated axon degeneration. *Brain* **131**, 1464-1477 (2008).

2 Duncan, I., Brower, A., Kondo, Y., Curlee, J. & Schultz, R. Extensive remyelination of the CNS leads to functional recovery. *PNAS* **106**, 6832-6836 (2009).

3 Murray, P., McGavern, D., Sathornsumetee, S. & Rodriguez, M. Spontaneous remyelination following extensive demyelination is associated with improved neurological function in a viral model of multiple sclerosis. *Brain* **124**, 1403-1416 (2001).

4 Kang, S. H. *et al.* Degeneration and impaired regeneration of gray matter oligodendrocytes in amyotrophic lateral sclerosis. *Nature Neuroscience* **16**, 571-579, doi:10.1038/nn.3357 (2013).

5 Franklin, R. J. M. Why Does Remyelination Fail in Multiple Sclerosis? *Nature Reviews Neuroscience* **3**, 705-714, doi:10.1038/nrn917 (2002).

6 Totoiu, M. O. & Kierstead, H. S. Spinal Cord Injury Is Accompanied by Chronic Progressive Demyelination. *The Journal of Comparative Neurology* **486**, 373-383 (2005).

7 Frakes, A. *et al.* Microglia induce motor neuron death via the classical NF-κB pathway in amyotrophic lateral sclerosis. *Neuron* **81**, 1009-1023 (2014).

8 Miron, V. *et al.* M2 microglia and macrophages drive oligodendrocyte differentiation during CNS remyelination. *Nature Neuroscience* **16**, 1211-1218, doi:10.1038/nn.3469 (2013).

9 Zrzavy, T. *et al.* Loss of 'homeostatic' microglia and patterns of their activation in active multiple sclerosis. *Brain* **140**, 1900-1913 (2017).

10 Kigerl, K. *et al.* Identification of two distinct macrophage subsets with divergent effects causing either neurotoxicity or regeneration in the injured mouse spinal cord. *J Neurosci* **29**, 13435-13444 (2009).

11 Lewis, N., Hill, J., Juchem, K., Stefanopoulos, D. & Modis, L. RNA sequencing of microglia and monocyte-derived macrophages from mice with experimental autoimmune encephalomyelitis illustrates a changing phenotype with disease course. *J Neuroimmunol* **277**, 26-38 (2014).

12 Yamasaki, R. *et al.* Differential roles of microglia and monocytes in the inflamed central nervous system. *J Exp Med* **211**, 1533-1549 (2014).

13 Mizutani, M. *et al.* The fractalkine receptor but not CCR2 is present on microglia from embryonic development throughout adulthood. *J Immunol* **188**, 29-36 (2012).

14 Vainchtein, I. D. *et al.* In acute experimental autoimmune encephalomyelitis, infiltrating macrophages are immune activated, whereas microglia remain immune suppressed. *Glia* **62**, 1724-1735, doi:10.1002/glia.22711 (2014).

15 Cusick, M., Libbey, J., Patel, D., Doty, D. & Fujinami, R. Infiltrating Macrophages Are Key to the Development of Seizures following Virus Infection. *J Virol* **87**, 1849-1860 (2013).

16 Mrdjen, D. *et al.* High-Dimensional Single-Cell Mapping of Central Nervous System Immune Cells Reveals Distinct Myeloid Subsets in Health, Aging, and Disease. *Immunity* **48**, 599, doi:10.1016/j.immuni.2018.02.014 (2018).

17 Bennett, F. C. *et al.* A Combination of Ontogeny and CNS Environment Establishes Microglial Identity. *Neuron* **98**, 1170-1183 e1178, doi:10.1016/j.neuron.2018.05.014 (2018).

18 Wlodarczyk, A. *et al.* A novel microglial subset plays a key role in myelinogenesis in developing brain. *EMBO J* **36**, 3292-3308 (2017).

19 Hagemeyer, N. *et al.* Microglia contribute to normal myelinogenesis and to oligodendrocyte progenitor maintenance during adulthood. *Acta Neuropathologica* **134**, 441-458 (2017).

20 Keren-Shaul, H. *et al.* A Unique Microglia Type Associated with Restricting Development of Alzheimer's Disease. *Cell* **169**, 1276-1290 (2017).

21 Krasemann, S. *et al.* The TREM2-APOE Pathway Drives the Transcriptional Phenotype of Dysfunctional Microglia in Neurodegenerative Diseases. *Immunity* **47**, 566-581 (2017).

22 Kotter, M., Setzu, A., Sim, F., Van Rooijen, N. & Franklin, R. Macrophage depletion impairs oligodendrocyte remyelination following lysolecithin-induced demyelination. *Glia* **35**, 204-212 (2001).

23 Lampron, A. *et al.* Inefficient clearance of myelin debris by microglia impairs remyelinating processes. *J Exp Med* **212**, 481-495 (2015).

24 Olah, M. *et al.* Identification of a microglia phenotype supportive of remyelination. *Glia* **60**, 306-321 (2012).

25 Hitomi, J. *et al.* Identification of a molecular signaling network that regulates a cellular necrotic cell death pathway. *Cell* **135**, 1311-1323, doi:10.1016/j.cell.2008.10.044 (2008).

26 Jouan-Lanhouet, S. *et al.* TRAIL induces necroptosis involving RIPK1/RIPK3-dependent PARP-1 activation. *Cell Death Differ* **19**, 2003-2014, doi:10.1038/cdd.2012.90 (2012).

27 Birgbauer, E., Rao, T. & Webb, M. Lysolecithin induces demyelination in vitro in a cerebellar slice culture system. *Journal of Neuroscience Research* **78**, 157-166 (2004).

28 Pan, Y. *et al.* Caspase-1 inhibition attenuates activation of BV2 microglia induced by LPS-treated RAW264.7 macrophages. *The Journal of Biomedical Research* **30**, 225-233 (2016).

29 Quarato, G. *et al.* Sequential Engagement of Distinct MLKL Phosphatidylinositol-Binding Sites Executes Necroptosis. *Molecular Cell* **61**, 589-601 (2016).

30 Vandenabeele, P., Galluzzi, L., Vanden Berghe, T. & Kroemer, G. Molecular mechanisms of necroptosis: an ordered cellular explosion. *Nature Reviews Molecular Cell Biology* **11**, 700-714, doi:doi:10.1038/nrm2970 (2010).

31 Lurbke, A. *et al.* Limited TCF7L2 Expression in MS Lesions. *PLOS one* **8** (2013).

32 Lewis, N., Hill, J., Juchem, K., Stefanopoulos, D. & Modis, L. RNA sequencing of microglia and monocyte-derived macrophages from mice with experimental autoimmune encephalomyelitis illustrates a changing phenotype with disease course. *Journal of Neuroimmunology* **277**, 26-38 (2014).

33 Mei, F. *et al.* Accelerated remyelination during inflammatory demyelination prevents axonal loss and improves functional recovery. *eLIFE* (2016).

34 Degterev, A. *et al.* Identification of RIP1 kinase as a specific cellular target of necrostatins. *Nature Chemical Biology* **4**, 313-321 (2008).

35 Remijsen, Q. *et al.* Depletion of RIPK3 or MLKL blocks TNF-driven necroptosis and switches towards a delayed RIPK1 kinase-dependent apoptosis. *Cell Death Dis* **5**, e1004, doi:10.1038/cddis.2013.531 (2014).

36 Ofengeim, D. *et al.* Activation of necroptosis in multiple sclerosis. *Cell Reports* **10**, 1836-1849 (2015).

37 Cassamo, A. *et al.* Necroptosis activation in Alzheimer's Disease. *Nature Neuroscience* doi:10.1038/nn.4608 (2017).

38 Kotter, M. R., Zhao, C., van Rooijen, N. & Franklin, R. J. Macrophage-depletion induced impairment of experimental CNS remyelination is associated with a reduced oligodendrocyte progenitor cell response and altered growth factor expression. *Neurobiol Dis* **18**, 166-175, doi:10.1016/j.nbd.2004.09.019 (2005).

39 Marin-Teva, J. L. *et al.* Microglia promote the death of developing Purkinje cells. *Neuron* **41**, 535-547 (2004).

40 Sun, L. *et al.* Mixed lineage kinase domain-like protein mediates necrosis signaling downstream of RIP3 kinase. *Cell* **148**, 213-227, doi:10.1016/j.cell.2011.11.031 (2012).

41 Zhao, J. *et al.* Mixed lineage kinase domain-like is a key receptor interacting protein 3 downstream component of TNF-induced necrosis. *Proc Natl Acad Sci U S A* **109**, 5322-5327, doi:10.1073/pnas.1200012109 (2012).

42 Bruttger, J. *et al.* Genetic Cell Ablation Reveals Clusters of Local Self-Renewing Microglia in the Mammalian Central Nervous System. *Immunity* **43**, 92-106 (2015).

43 Elmore, M. *et al.* Colony-stimulating factor 1 receptor signaling is necessary for microglia viability, unmasking a microglia progenitor cell in the adult brain. *Neuron* **82**, 380-397 (2014).
44 Huang, Y. *et al.* Repopulated microglia are solely derived from the proliferation of residual microglia after acute depletion. *Nat Neurosci*, doi:doi:10.1038/s41593-018-0090-8 (2018).
45 Moyon, S. *et al.* Demyelination causes adult CNS progenitors to revert to an immature state and express immune cues that support their migration. *J Neurosci* **35**, 4-20, doi:10.1523/JNEUROSCI.0849-14.2015 (2015).
46 Raine, C. S. & Wu, E. Multiple sclerosis: remyelination in acute lesions. *J Neuropathol Exp Neurol* **52**, 199-204 (1993).
47 Patani, R., Balaratnam, M., Vora, A. & Reynolds, R. Remyelination can be extensive in multiple sclerosis despite a long disease course. *Neuropathol Appl Neurobiol* **33**, 277-287, doi:10.1111/j.1365-2990.2007.00805.x (2007).
48 Wolswijk, G. Oligodendrocyte precursor cells in the demyelinated multiple sclerosis spinal cord. *Brain* **125**, 338-349 (2002).
49 Hammond, T. R. *et al.* Single-Cell RNA Sequencing of Microglia throughout the Mouse Lifespan and in the Injured Brain Reveals Complex Cell-State Changes. *Immunity*, doi:10.1016/j.immuni.2018.11.004 (2018).
50 Elmore, M. R. P. *et al.* Replacement of microglia in the aged brain reverses cognitive, synaptic, and neuronal deficits in mice. *Aging Cell* **17**, e12832, doi:10.1111/acel.12832 (2018).
51 Krukowski, K. *et al.* Temporary microglia-depletion after cosmic radiation modifies phagocytic activity and prevents cognitive deficits. *Sci Rep* **8**, 7857, doi:10.1038/s41598-018-26039-7 (2018).
52 Rice, R. A. *et al.* Microglial repopulation resolves inflammation and promotes brain recovery after injury. *Glia* **65**, 931-944, doi:10.1002/glia.23135 (2017).
53 Rubino, S. J. *et al.* Acute microglia ablation induces neurodegeneration in the somatosensory system. *Nat Commun* **9**, 4578, doi:10.1038/s41467-018-05929-4 (2018).
54 Grabert, K. & McColl, B. W. Isolation and Phenotyping of Adult Mouse Microglial Cells. *Methods Mol Biol* **1784**, 77-86, doi:10.1007/978-1-4939-7837-3_7 (2018).
55 Tay, T. L., Sagar, Dautzenberg, J., Grun, D. & Prinz, M. Unique microglia recovery population revealed by single-cell RNAseq following neurodegeneration. *Acta Neuropathol Commun* **6**, 87, doi:10.1186/s40478-018-0584-3 (2018).

Acknowledgements:

This work was funded by a Biotechnology and Biological Sciences Research Council (BBSRC)-Collaborative Award in Science and Engineering (CASE) studentship in collaboration with GlaxoSmithKline (V.E.M., J.C.R.; BB/M502777/1), a Medical Research Council and United Kingdom Multiple Sclerosis Society Career Development Award (V.E.M.; MR/M020827/1), funds from the Medical Research Council Centre for Reproductive Health (MR/N02256/1) and the Wellcome Trust (J.W.P.; 101067/Z/13/Z), and a Momentum Award from the United Kingdom Dementia Research Institute (J.P.). The cuprizone studies were supported by the German Research Foundation (T.K.; SFB-TR128-B7). The *Cx3cr1*-CreER experiments were supported by the German Research Foundation (J.P.; SFB-TR167). The LNC studies were supported by grants from F.R.S.-FNRS (A.d.R. and Y.L.), the Fondation Charcot Stichting and the International Foundation for Research in Paraplegia (IRP) (A.d.R.). We thank the United Kingdom Multiple Sclerosis Society Tissue Bank for providing MS tissue, Dr. F. Roncaroli (Imperial College London) for neuropathological diagnosis of MS lesions, and Dr. R. Nicholas (Imperial College j) for providing clinical history of MS patients. We also thank I. Molina-Gonzalez, Makis Tzioras, Neil Fullerton, C. Watkins, Dr. C. Böttcher, and J.Jamal El-Din for technical support, and Dr. Owen Dando for helpful discussions. A.F.L.'s salary and experiments for this study were funded by GlaxoSmithKline. J.C.R. was a full time employee at GlaxoSmithKline at the time of the study.

Author contributions:

A.F.L. co-designed the study, carried out the experiments, analysed and interpreted the data, and wrote the manuscript; C.L.D. carried out lesioning experiments, optimized lesion isolation protocols, assisted with flow cytometry, and performed experiments and analysis for RNA sequencing; R.K.H. assisted in lesioning experiments and optimized human tissue staining and analysis protocols; Y.L., D.C., and A.d.R. developed and tested LNCs for microglia targeting; G.I. assisted with genotyping; A.D and D.S. developed remyelination index quantification protocols; E.B. and A.W. provided corpus callosum lesion tissue; J.C.R. provided guidance for experimental design; A.W. and J.W.P. co-supervised the project, assisted with experimental design and interpretation, and manuscript editing;

T.K. provided cuprizone tissue and edited the manuscript; A.W. provided human tissue neuropathological mapping; J.P. assisted in experimental design, data interpretation, and manuscript editing; V.E.M. co-designed the study, supervised the project, and guided experimental design, data interpretation, and manuscript preparation.

Competing financial interests:

A.F.L.'s salary and experiments for this study were co-funded by GlaxoSmithKline. J.C.R. was a full time employee at GlaxoSmithKline at the time of the study.

Materials and correspondence:

To be addressed to Veronique Miron, vmiron@ed.ac.uk.

Figures and Legends:

Figure 1

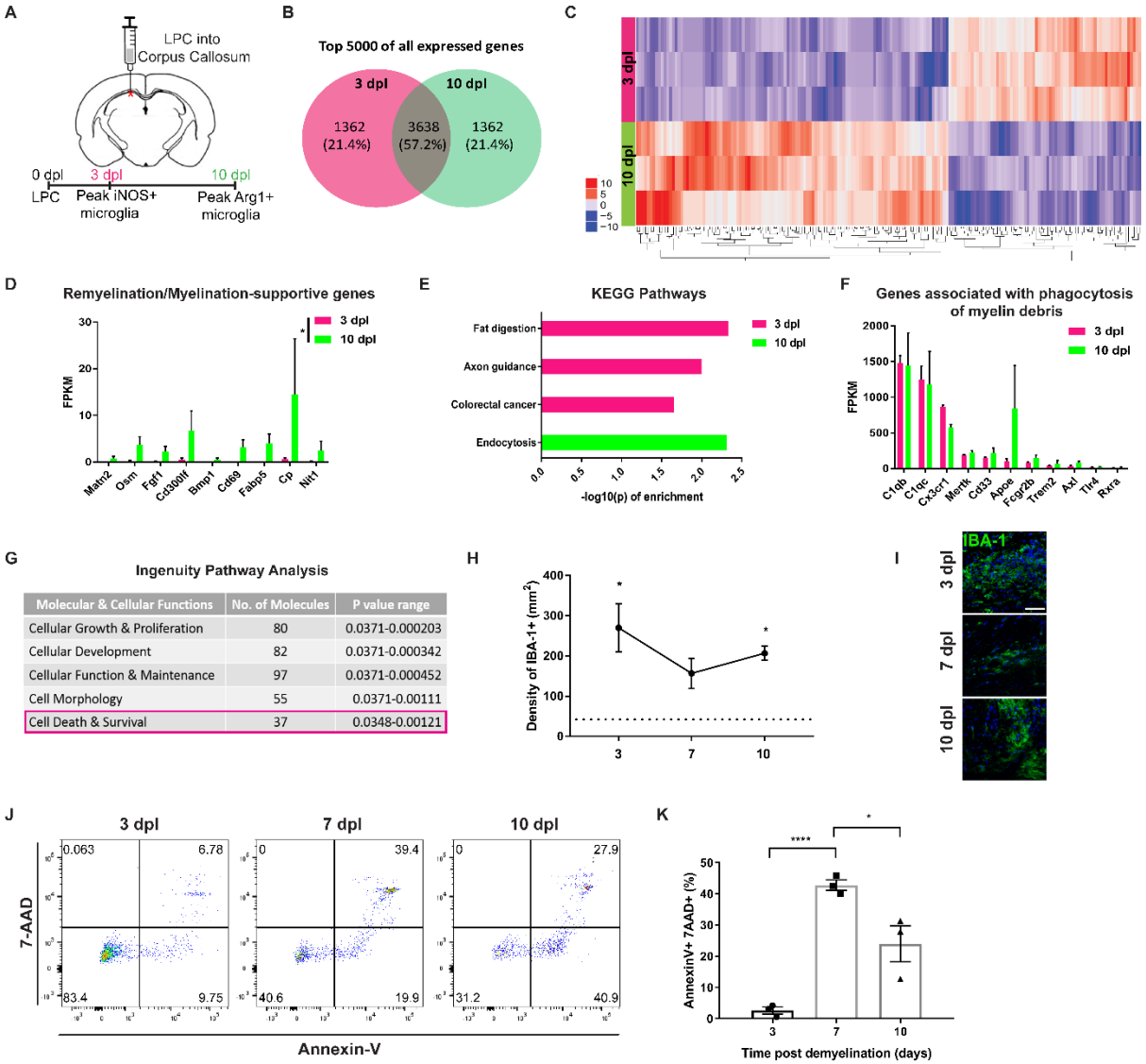

Molecular & Cellular Functions	No. of Molecules	P value range
Cellular Growth & Proliferation	80	0.0371-0.000203
Cellular Development	82	0.0371-0.000342
Cellular Function & Maintenance	97	0.0371-0.000452
Cell Morphology	55	0.0371-0.00111
Cell Death & Survival	37	0.0348-0.00121

Fig. 1. Microglia death occurs during transition in activation following *in vivo* demyelination.

A. Microglia were isolated from focal demyelinated lesions induced by LPC injection into adult mouse corpus callosum, at 3 and 10 dpl representative of key time points of microglial activation during remyelination, for subsequent RNA sequencing.

B. Overlap of top 5000 genes expressed by microglia (including non-significantly differentially expressed) at 3 and 10 dpl, ranked by average Fragments Per Kilobase of transcript per Million (FPKM).

C. Heat map of gene expression level per sample relative to average expression across all samples. Red represents higher expression and blue represents lower expression.

D. Genes with a significant Log_2 fold change ($p<0.05$) in 10 dpl vs 3 dpl microglia with known roles in regulating remyelination, myelination, and the oligodendrocyte lineage, represented as mean FPKM (± s.e.m.). *P=0.0174 (2-tailed paired Student's *t*-test).

E. Kyoto Encyclopedia of Genes and Genomes (KEGG) pathways engaged in genes significantly differentially expressed ($p<0.01$) by microglia at 3 vs 10 dpl. KEGG pathways are represented on the Y axis and enrichment score on the X axis represented as $-Log_{10}(p)$ enrichment ($p<0.05$).

F. Expression of genes associated with phagocytosis of myelin debris in microglia at 3 and 10 dpl, indicated as mean FPKM (± s.e.m.). No significance between time points, 2-tailed paired *t*-test.

G. Ingenuity Pathway Analysis of significantly engaged molecular and cellular functions in microglia ($p<0.05$), indicating 'Cell Death & Survival' as a key pathway.

H. Density of IBA-1+ cells per mm^2 (± s.e.m.) of lesioned corpus callosum at 3, 7, and 10 dpl. *P=0.0486 for 3dpl, 0.011 for 10 dpl (one sampled *t*-test compared to average density in sham-injected mice; indicated by the dotted line).

I. Representative images of lesions in the corpus callosum stained for IBA-1 (green) and counterstained with Hoechst (blue). Scale bar, 50 μm.

J. Flow cytometry plots of lesion-isolated microglia (Cd11b-PeCy7$^+$ Cd45-BV605^{lo}) positive for cell death markers Annexin-V-FITC and 7-AAD at 3, 7, and 10 dpl.

K. Mean proportion of all microglia which are Annexin-V+ 7-AAD+ at 3, 7 and 10 dpl ± s.e.m. ****P<0.0001 3dpl vs 7 dpl, *P=0.0233 7 dpl vs 10 dpl (2-tailed unpaired Student's *t*-test). N=3 mice/time point.

Figure 2

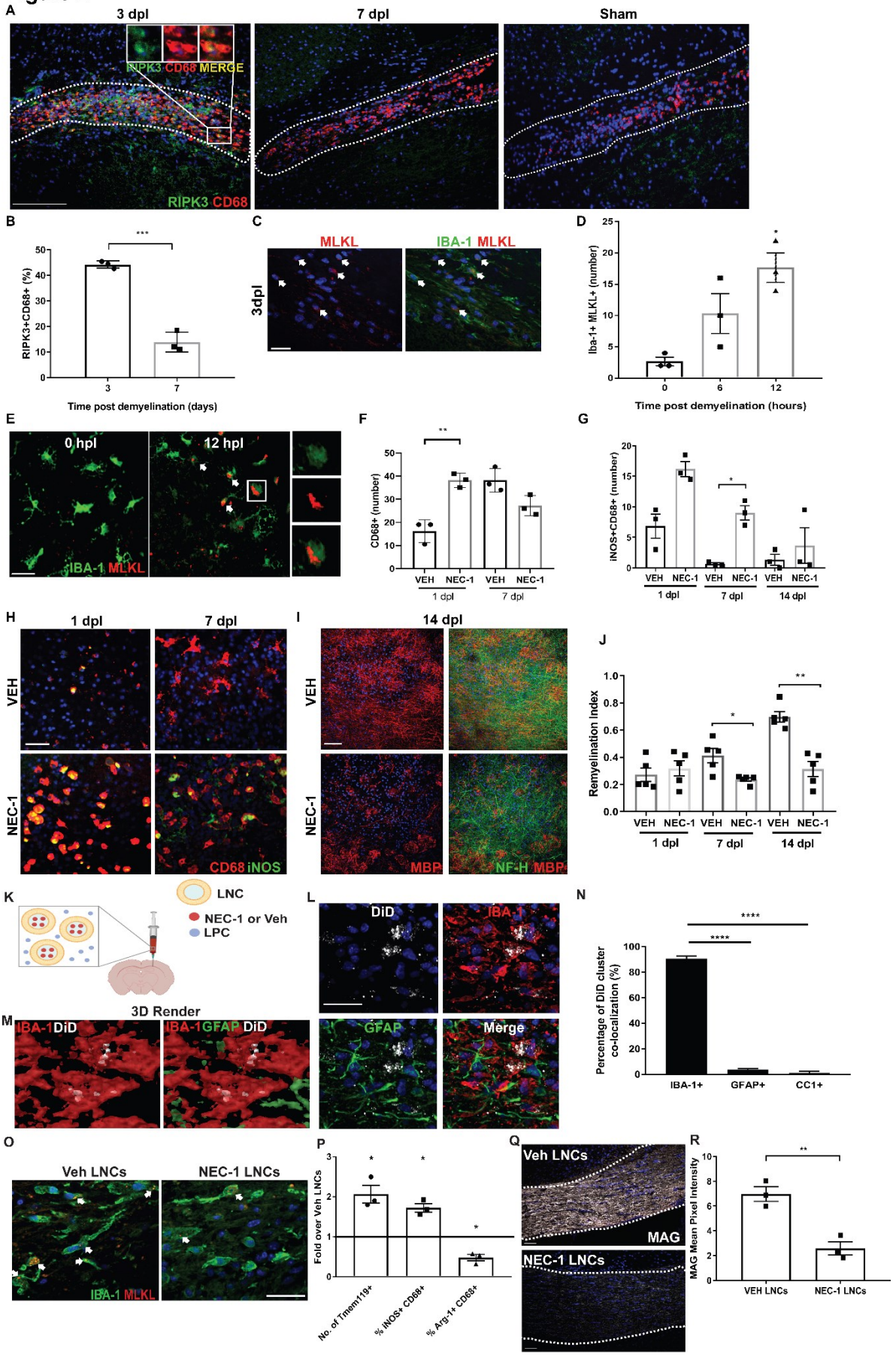
A
3 dpl
7 dpl
Sham
RIPK3 CD68 MERGE
RIPK3 CD68
B
RIPK3+CD68+ (%)
Time post demyelination (days)
C
MLKL
IBA-1 MLKL
3dpl
D
Iba-1+ MLKL+ (number)
Time post demyelination (hours)
E
0 hpl
12 hpl
IBA-1 MLKL
F
CD68+ (number)
VEH
NEC-1
1 dpl
7 dpl
G
iNOS+CD68+ (number)
14 dpl
H
1 dpl
7 dpl
VEH
NEC-1
CD68 iNOS
I
14 dpl
MBP
NF-H MBP
J
Remyelination Index
K
LNC
NEC-1 or Veh
LPC
L
DiD
IBA-1
GFAP
Merge
M
3D Render
IBA-1 DiD
IBA-1 GFAP DiD
N
Percentage of DiD cluster co-localization (%)
IBA-1+
GFAP+
CC1+
O
Veh LNCs
NEC-1 LNCs
IBA-1 MLKL
P
Fold over Veh LNCs
No. of Tmem119+
% iNOS+ CD68+
% Arg-1+ CD68+
Q
Veh LNCs
MAG
NEC-1 LNCs
R
MAG Mean Pixel Intensity
VEH LNCs
NEC-1 LNCs

Fig. 2. Pro-inflammatory microglia undergo necroptosis prior to onset of remyelination.

A. *In vivo* lesioned corpus callosum (dotted outline) at 3 and 7 dpl, along with a sham injection stained for RIPK3 (green) and CD68 (red). Inset at 3 dpl shows RIPK3+ CD68+ cell. Scale bar, 50µm.

B. Mean percentage of RIPK3+ CD68+ microglia / total CD68+ microglia at 3 and 7 dpl in *in vivo* lesioned corpus callosum ± s.e.m.. ***P=0.0002 (2-tailed unpaired Student's *t*-test). N=3 mice per time point.

C. Images of *in vivo* corpus callosum lesion stained for MLKL (red) and IBA-1 (green) at 3 dpl. Arrows indicate MLKL+ IBA-1+ cells. Scale bar, 10µm.

D. Mean number of MLKL+ microglia (IBA-1+) at 0, 6 and 12 hpl in slices ± s.e.m.. *p<0.05 12 hpl vs 0 hpl (Kruskal-Wallis test, Dunn's Multiple Comparison post-test). N=3 biological replicates.

E. Untreated (0 hpl) and LPC-treated slices (12 hpl) immunostained for IBA-1 (green) and MLKL (red), double positive cells indicated (arrows). Magnified example of a selected IBA-1+ MLKL+ cell (box; right) at 12 hpl. Scale bar, 10 µm.

F. Mean number of total microglia (CD68+) at 1 and 7 dpl in NEC-1- or VEH-treated slices ± s.e.m.. **P=0.0027 (2-tailed unpaired Student's *t*-test). N=3 biological replicates per time point and condition. Images taken at magnification 20X.

G. Mean number of iNOS+ microglia (CD68+) at 1, 7, and 14 dpl in NEC-1- or VEH-treated slices ± s.e.m.. *P=0.05 vs VEH (Mann-Whitney test). N=3 biological replicates per time point and condition.

H. Demyelinated slices treated with vehicle (VEH; left) or necrostatin-1 (NEC-1; right) at 1 and 7 dpl immunostained for CD68 (red) and iNOS (green). Scale bar, 20 µm.

I. Demyelinated slices treated with VEH (left) or NEC-1 (right) at 14 dpl immunostained for myelin (MBP; red) and axons (NF-H; green). Scale bar, 20 µm.

J. Remyelination index of VEH- and NEC-1-treated slices at 1, 7 and 14 dpl ± s.e.m.. *P=0.0159, **P=0.0079 vs VEH (Mann-Whitney test). N=5 biological replicates per time point and condition.

K. *In vivo* microglia-targeting of necrostatin (NEC-1) or vehicle control (Veh) using encapsulation in lipidic nanocapsules (LNC), co-injected with LPC into the corpus callosum.

L. Uptake of LNCs labelled with DiD (white) primarily by IBA-1+ cells (red) in lesioned corpus callosum *in vivo*, astrocytes (GFAP+) labelled in green. Scale bar, 10 µm.

M. 3D rendering of DiD-LNCs (white) internalized within IBA-1+ cells (red), astrocytes (GFAP+) labelled in green.

N. Percentage of DiD+ clusters (DiD-LNCs) in lesioned corpus callosum *in vivo* co-localized with microglia (IBA-1+), astrocytes (GFAP+), or oligodendrocytes (CC1+). ****P<0.0001 (2-tailed Student's *t*-test). N=3 mice.

O. Images of *in vivo* lesions at 3 dpl subsequent to treatment with Veh LNCs or NEC-1 LNCs, stained for IBA-1 (green) and MLKL (red). Scale bar, 10 µm.

P. Quantification of the number of Tmem119+ cells and percentage of iNOS+CD68+ or Arg-1+CD68+ (of total CD68+) in 10 dpl *in vivo* lesions subsequent to treatment with NEC-1 LNCs, represented as fold change over values in Veh LNC. *P=0.0395 for Tmem119+ cells, 0.026 for percentage of iNOS+CD68+ cells, and 0.0224 for percentage of Arg-1+CD68+ cells (One sample *t*-test compared to a hypothetical value of 1). N=3 mice per stain.

Q. Images of *in vivo* corpus callosum at 10 dpl (dotted outline) subsequent to treatment with Veh LNCs or NEC-1 LNCs stained for myelin protein MAG (white). Scale bar, 20 µm.

R. Mean MAG pixel intensity in *in vivo* lesions (with respective background intensity outside the lesion subtracted) at 10 dpl following injection with Veh LNCs or NEC-1 LNCs. **P=0.0055 (2-tailed unpaired Student's *t*-test). N=3 mice per condition.

386

Figure 3

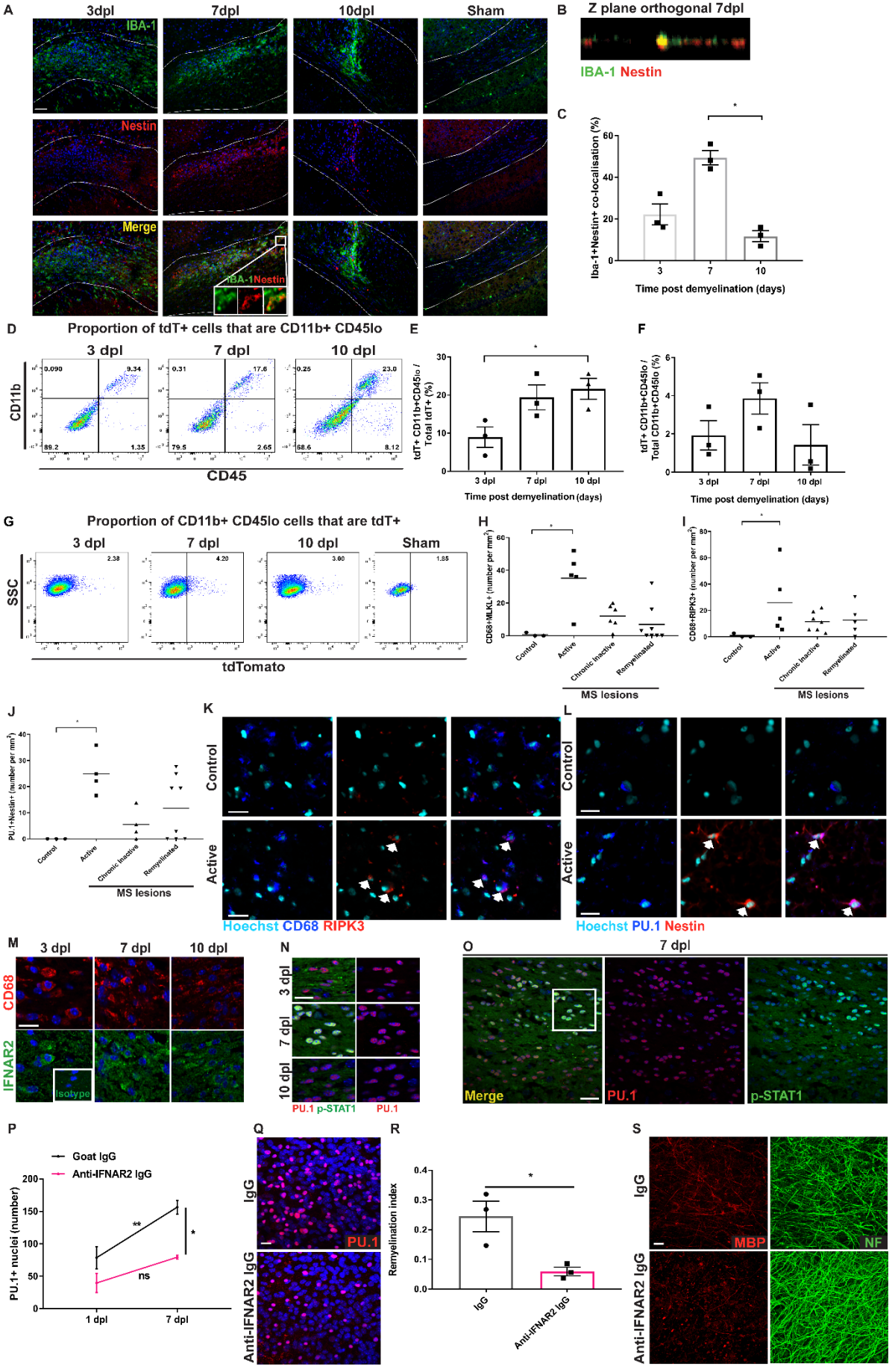
A
3dpl
7dpl
10dpl
Sham
IBA-1
Nestin
Merge
IBA-1Nestin
B
Z plane orthogonal 7dpl
IBA-1 Nestin
C
Iba-1+Nestin+ co-localisation (%)
Time post demyelination (days)
D
Proportion of tdT+ cells that are CD11b+ CD45lo
3 dpl
7 dpl
10 dpl
CD11b
CD45
E
tdT+ CD11b+CD45lo / Total tdT+ (%)
Time post demyelination (days)
F
tdT+ CD11b+CD45lo / Total CD11b+CD45lo (%)
Time post demyelination (days)
G
Proportion of CD11b+ CD45lo cells that are tdT+
Sham
SSC
tdTomato
H
CD68+MLKL+ (number per mm²)
Control
Active
Chronic Inactive
Remyelinated
MS lesions
I
CD68+RIPK3+ (number per mm²)
J
PU.1+Nestin+ (number per mm²)
K
Control
Active
Hoechst CD68 RIPK3
L
Hoechst PU.1 Nestin
M
CD68
IFNAR2
Isotype
N
PU.1 p-STAT1
PU.1
O
Merge
PU.1
p-STAT1
P
Goat IgG
Anti-IFNAR2 IgG
PU.1+ nuclei (number)
ns
Q
IgG
Anti-IFNAR2 IgG
R
Remyelination index
S
MBP
NF

Fig. 3. Microglia repopulation is associated with remyelination in mouse and human white matter and depends on Type-1 interferon signalling.

A. *In vivo* lesions of the corpus callosum (dotted line) at 3, 7 and 10 dpl, along with Sham PBS control (7 days post-surgery) stained for IBA-1 (green) and Nestin (red) Scale bar, 50µM. Inset at 7 dpl demonstrates zoom-in of co-localization of stains.

B. Z-plane orthogonal view of 7 dpl *in vivo* lesioned corpus callosum stained for Nestin (red) and IBA-1 (green) demonstrates co-expression.

C. Mean percentage co-localization between IBA-1 and Nestin *in vivo* staining normalized to total IBA-1 signal ± s.e.m.. *P=0.0219 7 dpl vs 10 dpl (Kruskal-Wallis test, Dunn's Multiple Comparison post-test). N=3 mice per time point.

D. Example plot of flow cytometric analysis of proportion of tdTomato+ cells within *in vivo* lesions which are $CD11b^{+}$ $CD45^{lo}$ at 3, 7, and 10 dpl.

E. Average percentage of tdTomato (TdT)+ cells ± s.e.m. which are $CD11b^{+}$ $CD45^{lo}$ at 3, 7, and 10 dpl *in vivo*. *P=0.0496 (One way ANOVA with post-hoc test). N=3 mice per time point.

F. Average percentage of $CD11b^{+}$ $CD45^{lo}$ cells ±s.e.m. which are tdTomato+ at 3, 7, and 10 dpl *in vivo*. N=3 mice per time point.

G. Example plot of flow cytometric analysis of proportion of $CD11b^{+}$ $CD45^{lo}$ cells which are tdTomato+ within *in vivo* lesions at 3, 7, and 10 dpl, compared to Sham PBS control.

H. Mean density of MLKL+ microglia (CD68+) per mm^2 in control, active, chronic inactive and remyelinated MS lesions. Individual data points represent separate lesions (see Supplementary Table 3). *P=0.0226 active lesions vs control (Mann-Whitney test).

I. Mean density of RIPK3+ microglia (CD68+) per mm^2 in control, active, chronic inactive and remyelinated MS lesions. Individual data points represent separate lesions (see Supplementary Table 1). *P=0.0357 active lesions vs control (Mann-Whitney test).

387

J. Mean density of Nestin+ PU.1+ cells per mm^2 in control, active, chronic inactive and remyelinated lesions. Individual data points represent separate lesions (see Supplementary Table 3). *P=0.0286 active lesions vs control (Mann-Whitney test).

K. Control brain tissue and active MS lesion immunostained for CD68 (blue) and RIPK3 (red), counterstained with Hoechst (turquoise). Scale bar, 20 µm.

L. Control brain tissue and active MS lesion immunostained for PU.1 (blue) and Nestin (red), counterstained with Hoechst (turquoise). Scale bar, 20 µm.

M. *In vivo* remyelinating lesions at 3, 7, and 10 dpl immunostained for CD68 (red) and IFNAR2 (green), counterstained with Hoechst (blue). Inset, rabbit primary isotype control. Scale bar, 10 µm.

N. *In vivo* remyelinating lesions at 3, 7, and 10 dpl immunostained for PU.1 (red) and phospho-STAT1 (green), counterstained with Hoechst (blue). Scale bar, 25 µm.

O. Representative image of focal *in vivo* lesion at 7 dpl immunostained for PU.1 (red) and phospho-STAT1 (green), counterstained with Hoechst (blue). White square corresponds to panel N. Scale bar, 25 µm.

P. Mean number of microglia (PU.1+) per field ± s.e.m. in *ex vivo* brain explants at 1 and 7 dpl, treated with anti-IFNAR2 neutralizing antibody or IgG control. N=3 per time point. **P=0.0098 Goat IgG 1dpl vs 7 dpl; *P=0.0103 Goat IgG 7 dpl vs anti-IFNAR2 IgG 7 dpl; One-way ANOVA and Sidak's multiple comparison, N=3 per time point.

Q. *Ex vivo* brain explants at 7 dpl treated with anti-IFNAR2 IgG or control IgG, immunostained for PU.1 (red) and counterstained with Hoechst (blue). Scale bar, 10 µm.

R. Mean remyelination index of *ex vivo* brain explants at 7 dpl ± s.e.m. treated with anti-IFNAR2 IgG or control goat IgG. *P=0.0252, 2-tailed Student's *t*-test. N=3 per condition.

S. *Ex vivo* brain explants at 7 dpl treated with anti-IFNAR2 IgG or control Goat IgG, immunostained for myelin basic protein (MBP; red) and neurofilament-H (NF; green), showing healthy early remyelination in control and debris in anti-IFNAR2 IgG treatment. Scale bar, 10 µm.